Using X-ray Computed Tomography to Describe the Dynamics of Nitrous Oxide Emissions during Soil Drying — Source link

Eva Rabot, Marine Lacoste, Catherine Hénault, Isabelle Cousin

Institutions: Institut national de la recherche agronomique

Topics: Soil structure and Hydric soil

Related papers:

- Effect of the soil water dynamics on nitrous oxide emissions

- Microbial hotspots and hot moments in soil: Concept & review

- Protection of soil carbon within macro-aggregates depends on intra-aggregate pore characteristics

- Challenges to incorporating spatially and temporally explicit phenomena (hotspots and hot moments) in denitrification models

- Can intra-aggregate pore structures affect the aggregate's effectiveness in protecting carbon?

Using X-ray Computed Tomography to Describe the Dynamics of Nitrous Oxide Emissions during Soil Drying

Eva Rabot, Marine Lacoste, Catherine Hénault, Isabelle Cousin

HAL Id: insu-01241590

https://hal-insu.archives-ouvertes.fr/insu-01241590

Submitted on 10 Dec 2015

Using X-ray computed tomography to describe the dynamics of nitrous oxide emissions during soil drying

1   **Using X-ray computed tomography to describe the dynamics of nitrous oxide emissions**

2   **during soil drying**

3   **E. Rabot[1,2], M. Lacoste[2], C. Hénault[2], I. Cousin[2,*]**

4   [1] Laboratoire Léon Brillouin, UMR12, CEA Saclay, 91191 Gif-sur-Yvette Cedex, France

5   [2] INRA, UR0272, UR Science du Sol, F-45075 Orléans, France

6   * Corresponding author: isabelle.cousin@orleans.inra.fr

7   **Impact statement**

8   We proposed a methodology to image the water dynamics and the soil structure of a soil

9   sample with X-ray computed tomography, while controlling the hydric state and monitoring

10   N_2O fluxes. Relevant information about N_2O transport could be extracted from the images.

11   **Abstract**

12   Water in soil is known to be a key factor for controlling nitrous oxide (N_2O) emissions,

13   because N_2O is mainly produced by denitrification in anoxic environments. In this study, we

14   proposed a methodology to image the water and soil structure of a soil sample with X-ray

15   computed tomography, while controlling the hydric state and monitoring N_2O fluxes. We

16   used a multistep outflow system to apply two wetting-drying cycles to an undisturbed soil.

17   The soil core was scanned with coarse-resolution X-ray computed tomography, one time

18   during wetting and several times during drying, to measure quantitative and qualitative

19   indicators of the pore network. Nitrous oxide emissions were higher during the first (C1) than

20   during the second (C2) wetting-drying cycle, both for the wetting and the drying phases.

21   Fluxes increased quickly after the beginning of the drying phase to reach a peak after 5 h.

22   Differences in the intensity of N_2O emissions between the two cycles were attributed to

23   differences in the water saturation, air-phase connectivity, and relative gas diffusion

24   coefficient, which led to more or less N_2O production, consumption, and entrapment in soil.

25   The speed of the N_2O emissions at the beginning of the drying phase depended on the rate of

26   increase of the air-filled pore volume and connectivity, and was especially well described by

27   the estimated relative gas diffusion coefficient. Parameters of the soil structure were not able

28   to explain completely the intensity of N_2O emissions during drying: N_2O production and

29   consumption factors were also involved.

30   **Abbreviations:** C1: first wetting-drying cycle; C2: second wetting-drying cycle; WFPS:

31   water filled pore space.

1   Introduction

33   Nitrous oxide (N_2O) concentration in the atmosphere is constantly increasing (Khalil et al.,

34   2002). With a global warming potential 300 times higher than that of carbon dioxide over a

35   100-year time scale (World Meteorological Organization, 2007), N_2O is the gas with the third

36   largest contribution to global warming (Ciais et al., 2013). Nitrous oxide plays also an

37   important role in the stratospheric ozone depletion (Ravishankara et al., 2009). Soils are a

38   major source of N_2O, accounting for 60% of natural sources (soils under natural vegetation)

39   and 60% of anthropogenic sources (soils used for agriculture; Ciais et al., 2013). Nitrous

40   oxide is produced during the natural microbial reactions of nitrification and denitrification,

41   two reactions which are controlled by the status of aerobiosis in soils. Since the water

42   saturation of soils modifies the ratio between water-filled and air-filled pore space, the water-

43   filled pore space (WFPS) is often used as an indicator of N_2O emissions (Butterbach-Bahl et

44   al., 2013; Robertson, 1989). In particular, wetting and drying cycles are known to affect N_2O

45   emissions (Guo et al., 2014; Muhr et al., 2008). Peaks of N_2O emissions have often been

46   observed both in the field and in laboratory experiments after the rewetting of a soil

47   (Groffman and Tiedje, 1988; Sanchez-Martin et al., 2010; Sexstone et al., 1985).

48   Following the model proposed by Smith (1980), N_2O production can occur inside anoxic

49   aggregates and then diffuse to the soil surface through inter-aggregate pores. Thus, delays

50   between microbial production and the moment when N_2O can be measured at the soil surface

51   have been demonstrated (Clough et al., 1998; McCarty et al., 1999; Rabot et al., 2014; Weier

52   et al., 1993; Wollersheim et al., 1987). Delays in N_2O emissions are partly linked to gas

53   entrapment and the associated dissolution of N_2O in the water phase (Clough et al., 2005). We

54   hypothesize here that introducing dynamic indicators of the soil structure could enhance our

55   understanding of the dynamic nature of N_2O emissions during wetting and drying cycles, by a

56   better description of N_2O transport. Indeed, since soil structure controls the water and gas

57   dynamics in soils, and thus the aerobic microbial activity, soil structure is supposed to be of

58   great importance for N_2O emissions (Ball, 2013).

59   Both the soil water and soil structure can be studied by X-ray computed tomography. X-ray

60   computed tomography is rapid, non-destructive, and allows successive scans over time while

61   measuring other dynamic parameters, such as N_2O fluxes. It provides 3-D images, used to

62   perform spatial analysis of the soil sample. In soil science, X-ray computed tomography is a

63   common tool, used for example to study the effect of agricultural practices (Deurer et al.,

64   2009; Schjønning et al., 2013; Schlüter et al., 2011), the water dynamics (Kasteel et al., 2000;

65   Sammartino et al., 2012; Wildenschild et al., 2005), or the gas dynamics (Deurer et al., 2009;

66   Katuwal et al., 2014; Naveed et al., 2013). Katuwal et al. (2014) demonstrated the interest of

67   coarse-resolution X-ray scanners to study gas transport functioning in macropores. This

68   methodology can be applied to N_2O emissions. Only few studies used imaging techniques to

69   study greenhouse gas emissions (e.g., Mangalassery et al., 2014; Mangalassery et al., 2013),

70   and to our knowledge, none of them monitored greenhouse gases while acquiring images of

71   the soil structure.

72   In this study, we proposed a methodology to image the water and soil structure of a soil

73   sample with coarse-resolution X-ray computed tomography, while controlling the hydric state

74   and monitoring N_2O fluxes. We aimed at demonstrating which relevant information can be

75   extracted from the images to allow a better understanding of N_2O emissions. We illustrated

76   this methodology by subjecting a soil sample to two wetting and drying cycles.

77   **2   Material and methods**

78   **2.1   Soil sampling, physical and chemical characterization**

79   The study site was chosen for the high N_2O emissions previously recorded in the field (Gu et

80   al., 2011), at the same location as the study of Rabot et al. (2014). The site is an agricultural

81   field cultivated with rape (*Brassica napus* L.), located near Chartres, in the northwest of

82   France (48.376° N lat, 1.196° E long). The soil is classified as Glossic Retisol (WRB, 2014),

83   with a clay content of 13.7%, a silt content of 82.0%, and a sand content of 4.3% (Rabot et al.,

84   2014). A soil core was collected in June 2013 in a PVC cylinder (13.2-cm inner diameter by

85   7-cm height) from the surface horizon (1–8 cm). Bulk soil was also sampled in the surface

86   horizon for physical and chemical analyses. Soil organic carbon was measured by

87   sulfochromic oxidation, and total nitrogen was measured by the Dumas method. The soil

88   nitrate content was determined by colorimetric analysis after the extraction from an 8-g soil

89   sample using 0.5 M K_2SO_4. Soil pH was determined in a 1:2.5 soil/water volume ratio on

90   samples sieved at < 2 mm. At the sampling time, the soil organic carbon was 9.5 g kg^{-1}, the

91   total nitrogen content was 0.91 g kg^{-1}, the nitrate content was 51.3 mg NO_3^-–N kg^{-1}, and the

92   soil pH was 5.6. The porosity of the soil sample was 0.46 cm^3 cm^{-3} and the volumetric water

93   content was 37.7% (equivalent to 81.9% WFPS). The sample was conditioned in a plastic bag

94   and stored field moist during two weeks at 5°C to minimize microbial activity. Before the

95   start of the experiment, the soil core was trimmed on each end and maintained at 20°C for 24

96   h.

97   **2.2   Experimental setup**

98   The experiment consisted in controlling the hydric status of the soil sample with a multistep

99   outflow system (Weihermüller et al., 2009): the soil cylinder was connected to a water-tank to

100   control its wetting according to the Mariotte bottle principle, and connected to a vacuum

101   pump and a sampling bottle to control its drying (Fig. 1). Hydraulic continuity was ensured

102   with a porous ceramic plate (1-bar air-entry value, 8.6×10^{-8} m s^{-1} saturated hydraulic

103   conductivity, Soilmoisture Equipment Corp.) placed at the bottom of the soil cylinder and

104   previously saturated with water. The soil cylinder-ceramic plate system was sealed with

105   silicon to avoid water or gas leaks. Both the water content and water potential were

106   continuously monitored during the experiment, with a balance (0.1 g precision) and two

107   microtensiometers (porous ceramic cup, 20-mm length, 2.2-mm diam., 150-kPa air-entry

108   value) inserted at 2 and 4 cm from the cylinder surface at the end of the wetting phase. Data

109   were recorded every 10 min with a datalogger (CR1000, Campbell Scientific).

110   Two wetting-drying cycles (hereafter referred to as the C1 and C2 cycles) were applied to the

111   soil cylinder. The initial water content for C1 was the water content at sampling. The sample

112   was first saturated for 3 d by raising the water level to the soil surface in one step, and then a

113   -100 hPa pressure was applied at the bottom of the soil core in one step, and maintained for

114   about 7 h (C1 cycle). A zero hPa pressure was then applied for 3 d, followed by a -100 hPa

115   pressure for about 7 h (C2 cycle). Indeed, Rabot et al. (2014) demonstrated that N_2O peaks

116   can be created during the drying phase, at a matric potential of approximately -50 hPa. We

117   chose thus to apply a pressure lower than this value of -50 hPa. The speed of the matric

118   potential decrease was much higher that under natural conditions, and could affect the water

119   transport and hydraulic continuity. We used a KNO_3 solution as the wetting fluid, to ensure

120   that nitrate was not a limiting factor for N_2O emissions during the wetting phase, and to

121   isolate the effects of nitrate concentration and soil moisture on the N_2O emissions. Hénault

122   and Germon (2000) showed that the response of N_2O emissions to the nitrate concentration

123   could be described by a Michaelis-Menten function. We used a nitrate concentration at the

124   plateau of this function (4.1 mM N). The nitrate solution was prepared with de-aired water to

125   prevent air bubble formation during the experiment.

126 Nitrous oxide emissions were monitored by infrared correlation spectroscopy (N_2O Analyzer

127 model 46i, Thermo Scientific) using a 4-L volume closed-chamber. The emissions were

128 measured for 20-min periods, and the concentration value was recorded every minute. Given

129 the linear increase of the N_2O concentration in the closed-chamber, N_2O fluxes were

130 calculated linearly from the observed change in concentration during the first 10 min after the

131 chamber was closed. Only one N_2O flux measurement was done during wetting, at the end of

132 each wetting phase for each cycle, and seven (respectively eight) flux measurements were

133 recorded during the drying phase for the C1 (respectively C2) cycle. Moreover, gases inside

134 the chamber were sampled in evacuated vials at the end of the wetting phase and at the middle

135 of the drying phase (3.5 h after the beginning of the drying phase), and CO_2 concentration was

136 determined by gas chromatography (μGC Gas Analyzer T-3000, SRA Instruments). For a

137 single CO_2 flux measurement, the atmosphere of the closed-chamber was sampled three times

138 during 20-min periods. Given the linear increase of the CO_2 concentration, the flux was then

139 calculated linearly. The chamber was removed before each measurement to restore the

140 atmosphere to ambient concentrations of gases. The sample was kept inside the scanner

141 during the two wetting-drying cycles. The temperature inside the scanner room was monitored

142 and ranged between 22.5 and 25.5°C throughout the experiment.

2.3   Computed tomography and image analyses

144 The soil sample was placed in the scanner in its sampling direction. The soil sample was

145 scanned one time at the end of the wetting phase, and the vacuum pump was then activated to

146 begin the soil drying. We then scanned the sample seven times for C1, and nine times for C2

147 during the drying phase, alternating with N_2O flux measurements. Two scans have been added

148 at C2 compared to C1 to refine the results just after the beginning of the drying phase. We

149 used a medical X-ray tomograph (Siemens Somatom Definition AS) operating at an energy

150 level of 200 kV and a current of 140 mA. The voxel size was $316 \times 316 \times 100$ μm. The scanning

151 duration was 15 seconds. In the following, intensities are expressed in Hounsfield units (HU).

152 Most of the image processing was realized with the ImageJ software (Rasband, 1997-2014).

153 Due to the chamber manipulation during the experiment and displacement of the sample

154 between scans, image registration was first done to ensure spatial consistency between the

155 different images with the Align3 TP plugin (Parker, 2012). We cropped the images to exclude

156 non-soil areas, and we rescaled the images to get isotropic voxels of 316 μm. The noise was

157 reduced by using a bilateral filter, and edges were enhanced with an unsharp mask (Schlüter

158 et al., 2014). The air phase and the water phase were both separated from the soil matrix and

159 gravels by using the watershed segmentation method. This method has previously been

160 successfully used to segment images of soils (Schlüter et al., 2014). A majority filter with a

161 $3 \times 3 \times 3$ kernel was applied to remove very small air-filled and water-filled pores which can be

162 seen as noise. We finally removed manually the signal of the two tensiometers. The procedure

163 used to segment the air phase and the water phase gave satisfactory results (Fig. 2).

164 Visualization of the air-filled and water-filled pore network was done with the ImageJ plugin

165 3-D Viewer (Schmid et al., 2010).

166 The volume of air-filled and water-filled macropores was estimated with the BoneJ plugin

167 (Doube et al., 2010), and the Euler number was calculated considering 26-connectivity with

168 the C library QuantIm v.4 (Vogel, 2008), on the segmented images. The Euler number

169 characterizes the connectivity of the air-filled pore space (Vogel et al., 2010). When the Euler

170 number is positive, the pore network is classified as unconnected, whereas it is connected

171 when the Euler number is negative. The volume of air-filled macropores and Euler number

172 were calculated on the total air-filled pores identified, and the air-filled pores connected to the

173 soil surface only, to evaluate the pore network contributing to N_2O emissions. We estimated

174 the relative gas diffusion coefficients D_S/D_0 from the segmented air-filled pore space with

175   QuantIm v.4 (Vogel, 2008), as already done by Deurer et al. (2009) and Vogel et al. (2002).

176   The gas diffusion was modeled by using the Fick's law of diffusion in 3-D, solved by explicit

177   finite differences. Throughout the simulation, the gas concentration at the bottom of the soil

178   sample was fixed at a constant value, and the gas concentration at the top was set to zero. We

179   calculated D_S/D_0 on subsamples of increasing thickness from the soil surface (adding 10

180   pixels at the bottom of the given subsample).

3   Results

3.1   Soil water content and soil water potential evolution

183   During the drying phase, the WFPS measured with the MSO system ranged between 85% and

184   79% at C1, and between 83% and 79% at C2. The soil matric potential was above 0 cm for

185   the two wetting cycles for the –4 cm depth tensiometer, whereas it was slightly under 0 cm for

186   the –2 cm depth tensiometer at C2 (Fig. 3). Saturation was thus slightly lower during C2. The

187   matric potential showed a plateau at the C2 wetting phase, reached in approximately 4.5 h

188   after the beginning of the C2 wetting phase. During the drying phase, the matric potential

189   decreased linearly, immediately after activating the vacuum pump, to reach –56 cm water

190   column at C1 and –67 cm water column at C2. The decrease of the matric potential was

191   slightly faster at C2 than at C1 (mean decrease of –8.8 cm h^{-1} at C1, and –9.5 cm h^{-1} at C2).

3.2   Dynamics of the N_2O and CO_2 fluxes

193   Emissions were lower during C2 than during C1, both for the wetting and the drying phases,

194   with the maximum N_2O flux being 55.1 mg N m^{-2} d^{-1} at C1, and 19.1 mg N m^{-2} d^{-1} at C2

195   (Fig. 3). Nitrous oxide fluxes were measured to be 9.4 and 0.1 mg N m^{-2} d^{-1} at the end of the

196   C1 and C2 wetting phase, respectively. In comparison, they ranged between 0 and 2.6 mg N

197   m^{-2} d^{-1} in the field measurements of Gu et al. (2011) on the same study site. Nitrous oxide

198 fluxes increased quickly during the drying phase to reach a peak approximately 5.5 h after the

199 beginning of the soil drying at C1, and 4.5 h at C2. Peaks occurred at a mean matric potential

200 of –41.1 cm water column at C1, and –44.7 cm at C2, and at a WFPS of 80.2% at C1 and

201 80.5% at C2. The increase in the N_2O fluxes was faster for C1 than for C2. The first flux

202 measurement of C1 was especially high (38.2 mg N m^{-2} d^{-1}) compared to the following

203 measurements. At C2, the fluxes measured at the beginning of the drying phase increased

204 more slowly, with fluxes between 3.3 and 3.9 mg N m^{-2} d^{-1} for the three first measurements.

205 Carbon dioxide fluxes were higher at C2 than at C1 at the end of the wetting phase (50.4 mg

206 CO_2 m^{-2} d^{-1} at C1, and 164.1 mg CO_2 m^{-2} d^{-1} at C2). An opposite trend was observed during

207 the drying phase: CO_2 fluxes were higher at C1 than at C2 (108.3 mg CO_2 m^{-2} d^{-1} at C1, and

208 76.1 mg CO_2 m^{-2} d^{-1} at C2). Soil pH at the end of the two wetting-drying cycles was 5.9.

209 **3.3   Characterization of the pore network**

210 Four components could be identified, both visually and in the histograms of each image: air

211 phase, water phase, soil matrix, and gravels (Fig. 4 and 5). We define the soil matrix as the

212 solid phase and pores with a size lower than the image resolution. Histograms appeared to be

213 unimodal, with the mode corresponding to the soil matrix, because the air-filled and water-

214 filled porosities represented only a small fraction of the soil sample volume (Fig. 4a and 4b).

215 A small peak near the pure air intensity value (–1024 HU) could be identified for the drying

216 phase, and a small peak near the pure water intensity value (0 HU) could be identified for the

217 wetting phase (Fig. 4c and 4d). Less water voxels and more air voxels were identified at C2

218 than at C1 during the wetting phase, showing that the water saturation was lower at C2 (Fig.

219 4c and 4d).

220 A 3-D rendering of the air phase and water phase distributions at the end of the wetting phase

221 and at the end of the drying phase for C1 and C2 is given in Fig. 5. Cylindrical pores,

222   probably earthworm burrows and root channels (of which one major root channel of

223   approximately 9 mm diameter), as well as smaller pores attributed to inter-aggregate voids are

224   visible. As expected, air-filled pores appeared to be more numerous at the end of the drying

225   phase than at the end of the wetting phase. A high volume of pore remained not saturated

226   during the experiment.

227   Most of the indicators calculated from the segmented images were highly correlated, except

228   the Euler number and D_S/D_0 (Table 1). Indeed, largest pores highly contributed to the

229   porosity, but relatively little to Euler number (Vogel et al., 2002), and D_S/D_0 includes

230   additional information about the tortuosity. The air-filled porosity identified ranged between

231   0.029 and 0.035 cm^3 cm^{-3} at C1, and between 0.023 and 0.035 cm^3 cm^{-3} at C2. In the driest

232   scan of C2, where the maximum air-filled pore volume has been identified, this air-filled

233   porosity is equivalent to 16% of the real air-filled porosity at a pressure of –100 hPa, or 7.5%

234   of the total porosity (0.46 cm^3 cm^{-3}). For the total core volume, time-evolution of the air-

235   filled pore volume showed a rapid rise from the beginning to 1 h after the soil drying, and

236   then the system entered a state of equilibrium (Fig. 6a). C1 and C2 followed the same trend,

237   but the air-filled pore volume was significantly higher at C2 than at C1 at the end of the

238   wetting phase, and slightly higher at C2 than at C1 during the drying phase. The volume of

239   water-filled pores decreased quickly in the first hour of soil drying, and remained lower at C2

240   than at C1 during the whole experiment (Fig. 6a). The evolution of the air-filled pores

241   connected to the soil surface showed the same trend as for the total core volume, except that

242   no more difference can be seen between C1 and C2 after 2 h of soil drying (Fig. 6c).

243   For the total air-filled pore volume identified, the Euler number ranged between 1319 and

244   1849 at C1, and between 1405 and 1713 at C2 (Fig. 6b). Thus, the Euler number was positive

245   during the whole experiment, meaning that the air-filled pore network was unconnected at the

246   resolution of the images. The Euler number was lower at C2 than at C1 during the wetting

247   phase, and higher at C2 than at C1 during the drying phase. The air-filled pore connectivity

248   was thus better at C1 during the drying phase. The value of the Euler number tended to

249   decrease with soil drying. For the air-filled pores connected to the soil surface only, the Euler

250   number ranged between −52.5 and 17 at C1, and between −57 and 1 at C2 (Fig. 6d). A

251   transition between an unconnected and a connected pore network occurred in the first hour of

252   soil drying: the Euler number was positive at the end of the wetting phase, and negative

253   during the drying phase. The inherent connectivity improved then as the soil dried. The Euler

254   number was higher at C1 than at C2 during the whole experiment. One major pore cluster,

255   representing 98% of the air-filled pore volume connected to the soil surface at the end of the

256   two drying phases, was responsible for the negative value of the Euler number. The other

257   pores were smaller and had a less complicated morphology.

258   Simulated relative gas diffusion coefficients were null for subsamples thicker than

259   approximately 3 cm at C1, and 4 cm at C2, because deepest pores were poorly connected to

260   the soil surface. Thus, only the upper part of the soil sample could participate to the fast N_2O

261   transport to the soil surface in the gaseous phase. The evolution with time of the gas diffusion

262   coefficient of a 3-cm-thick subsample is given in Fig. 7. Absolute values of D_S/D_0 ranged

263   between 0.000 and 0.009 at C1, and between 0.003 and 0.005 at C2. They were higher at C2

264   than at C1, except for the first measurement of the C1 drying phase. Relative gas diffusion

265   coefficients increased quickly after the beginning of the soil drying at C1, and then showed

266   lower values. This peak at C1 was concomitant with a fast increase of the N_2O flux. The

267   increase with soil drying was slower at C2 than at C1. Trends were similar for the estimation

268   of D_S/D_0 on thinner subsamples (data not shown).

269   **4   Discussion**

270   **4.1   The use of X-ray computed tomography for greenhouse gas emission studies**

271   The experiment of the present study appeared as the first report of coupling between soil

272   imaging, greenhouse gas flux measurements, and hydric control measured on the same

273   sample. The use of X-ray computed tomography allowed identifying spatially the water and

274   gas phases in the macropores, and thus determining the air-filled pore volume of these

275   macropores at successive moments during the soil drying. At the scanner resolution, only 16%

276   of the real air-filled porosity was identified, and the rest remained unresolved. Indeed, we

277   used a large sample, with a size typical of that used to determine soil hydraulic properties, to

278   approach the representative elementary volume of the soil. The pixel size was thus coarse,

279   approximately 300 μm. With such a resolution, only macropores are unequivocally

280   recognized, i.e., pores > 300 μm with the nomenclature of Jarvis (2007). According to Young-

281   Laplace law (assuming 0° degree contact angle, interfacial tension for air-water and spherical

282   interfaces), these macropores are expected to drain at a water potential of –10 cm.

283   Identifying a higher range of pore sizes would have been informative since macropores

284   participate to N_2O transport, whereas N_2O production rather occurs in fine pores of the matrix

285   domain (Heincke and Kaupenjohann, 1999). However, such a coarse resolution has

286   successfully been used in previous studies to link soil structure and gas diffusion. By using X-

287   ray computed tomography at a resolution of approximately 500 μm, Katuwal et al. (2014)

288   observed a high positive correlation between air permeability and the air-filled macroporosity

289   identified in their images. Deurer et al. (2009) explained a major part of the variability of the

290   gas diffusion coefficients by the air-filled porosity and connectivity of pores > 300 μm

291   identified with imaging. In the present study, despite the significant fraction of the unresolved

292   pores which were air-filled at the end of the two drying cycles, coarse-resolution X-ray

293   computed tomography can be used to infer N_2O transport functioning. We also succeeded in

294   identifying differences in the soil moisture between the two wetting-drying cycles. This

295   difference was consistent with the other parameters recorded, i.e., matric potential and WFPS,

296   and allowed inferring differences in anoxia level in the soil profile between C1 and C2.

297   Relative, instead of absolute, comparisons between the two wetting-drying cycles could thus

298   be performed.

299   **4.2   Nitrous oxide emissions and pore connectivity**

300   After 3 days of water saturation, soil drying down to –45 cm water column induced maximum

301   N_2O fluxes. This result has been previously observed by Rabot et al. (2014). They

302   hypothesized that the gas diffusion coefficient increased as the soil dried and allowed the

303   release of the N_2O previously entrapped during the wetting phase in the pore space or in the

304   soil solution. Nitrous oxide entrapment in soils at high WFPS has already been highlighted in

305   laboratory experiments (Clough et al., 1998; McCarty et al., 1999; Weier et al., 1993). In this

306   new study, supplementary information about the soil structure was obtained and we were able

307   to measure an increase of the air-filled macropores connected to the soil surface as the soil

308   dried. The air-filled pore network connected to the soil surface was described as well

309   interconnected during the drying phase. Fast N_2O transport in the gaseous phase could occur

310   from the soil upper part connected to the atmosphere during the drying phase, where some

311   biological hotspots could be active (Ball et al., 2008; van der Weerden et al., 2012). The

312   porous network was probably also connected by pores of a size lower than the one recorded

313   by the X-ray scanner, which represent approximately 85% of the air-filled pore space at a

314   pressure of –100 hPa. The observed increase of the air-filled pore volume connected to the

315   soil surface, pore connectivity, and relative coefficient of gas diffusion with soil drying favors

316   the hypothesis of Rabot et al. (2014), stating that entrapped N_2O was released during the

317   drying phase.

318   By considering the whole pore volume, the pore network was classified as unconnected

319   during the experiment. Firstly, given that the value of the Euler number depends on the size of

320   the lower pore which can be resolved (Vogel et al., 2010), the soil sample may have been

321   connected by unresolved air-filled pores. With a coarse-resolution scanner, we underestimate

322   the connectivity of the soil sample. Secondly, the Euler number is a metrics highly affected by

323   isolated voxels (Renard and Allard, 2013), like unconnected structural pores or thresholding

324   artifacts, leading to highly positive values. Katuwal et al. (2014) observed that the Euler

325   number was not a good measure of macropore connectivity to compare soil samples.

326   Evolution of the Euler number for the whole identified pore volume is thus difficult to

327   interpret, especially as a large fraction of the pore space remained unresolved. We favor the

328   use of the Euler number for the pores connected to the soil surface, which, by construction,

329   includes less isolated pores. Despite a high computational cost, the estimation of D_S/D_0 from

330   the segmented pore network appeared to better describe N_2O transport, by showing an

331   evolution similar to that of N_2O fluxes: a fast increase at C1 and a slow increase at C2. The

332   relative gas diffusion coefficient provided comprehensive information, by taking into account

333   the pore network connectivity and tortuosity, and was less affected by isolated voxels.

334   **4.3   Intensity of nitrous oxide emissions**

335   By comparing the two wetting and drying cycles, differences in the amount of N_2O emitted

336   were observed. Emissions were lower at C2 than at C1 both during the wetting and the drying

337   phases. A lower water content at C2 may have been responsible for the lower N_2O production

338   during the C2 wetting phase. Moreover, the higher connectivity and relative gas diffusion

339   coefficient at C2 during the wetting phase caused lower N_2O entrapment in soil, and could

340   also explain the lower N_2O release during the C2 drying phase. Balaine et al. (2013)

341   suggested that N_2O emissions were low for $D_S/D_0 < 0.006$ in their experiment on repacked

342   soil samples at a hydric steady-state, because N_2O was entrapped in the soil and because the

343   reduction of N_2O into N_2 was high. The observations in our present study support these

344   findings, as we estimated values of $D_S/D_0 < 0.006$ during the wetting phase, and we observed

345   N_2O entrapment. Nitrous oxide reduction into N_2 is expected to occur two or three days after

346   the water saturation of a soil sample (Letey et al., 1980). Nitrous oxide consumption probably

347   occurred in the present study during the wetting phase, as WFPS > 90% favors this reaction

348   (Ruser et al., 2006). Small differences in WFPS between the wetting phases of C1 and C2

349   could have caused differences in N_2O consumption. In the literature, reduced N_2O production

350   after a second wetting and drying cycle has also been explained by the C and N dynamics in

351   relation to the microbial dynamics activity (Fierer and Schimel, 2002; Mikha et al., 2005;

352   Muhr et al., 2008). In our study, nitrate was supplied in excess during the wetting phase of

353   each wetting-drying cycle, so nitrate was supposed not to be limiting at the beginning of each

354   wetting-drying phase. On the contrary, the carbon dynamics can be implicated in the lower

355   emissions at C2. A shortage of C after a first wetting-drying cycle may have consumed easily

356   available C substrates (Fierer and Schimel, 2002), and/or less C substrates may have been

357   exposed to microbial consumption at C2, by the physical disruption of soil aggregates during

358   the wetting-drying cycles (Denef et al., 2001).

359   **4.4   Timing of nitrous oxide emissions**

360   In addition to the differences in terms of intensities of N_2O emissions between the two wetting

361   and drying cycles, differences in the timing of the N_2O peaks were also observed. The matric

362   potential appeared to be a good indicator of the timing of N_2O emissions, as already shown by

363   Castellano et al. (2010), because the matric potential defines the diameter of the water-filled

364   pores. We found that maximum N_2O fluxes were reached at approximately -45 cm water

365   column, that is to say when pores with diameter > 66 μm were drained. This is consistent with

366   the experiment of Castellano et al. (2010), who observed in their free drainage experiment

367   that N_2O peaks occurred when pores with diameter > 80 μm were drained. In the experiment

368   of Balaine et al. (2013), N_2O peaks were observed when pores with diameter > 197 and > 57

369   μm were drained, in soils repacked at bulk densities 1.1 and 1.5 g cm^{-3}, respectively.

370   The timing can also be compared between the two wetting-drying cycles. In our study, N_2O

371   fluxes were very high soon after the beginning of the C1 drying phase contrary to C2. Indeed,

372   less N_2O may have been produced during the C2 wetting phase, leading to a lower gas

373   concentration gradient between the soil surface and the atmosphere, and thus to a slower gas

374   diffusion. Moreover, the lower rate of increase at C2 than at C1 of the air-filled pore volume,

375   connectivity, and relative gas diffusion coefficient, at the beginning of the drying phase, could

376   also explain the slower N_2O emissions at the beginning of the C2 drying phase. These

377   variables were highly correlated, so only one of them could have been computed. The volume

378   of air-filled pores and the Euler number of pores connected to the soil surface were easily

379   calculated, but the relative gas diffusion coefficient appeared to be more efficient to describe

380   the timing of N_2O emissions.

381   **Conclusion**

382   We hypothesized that introducing dynamic indicators of the soil structure could enhance our

383   understanding of the dynamic nature of N_2O emissions by soils. The experiment performed in

384   this study was intended to demonstrate the ability of a coupling between coarse-resolution X-

385   ray computed tomography, hydric control and N_2O flux measurements, to better describe N_2O

386   transport in soils. X-ray computed tomography is a rapid and non-destructive method, which

387   allowed measuring an evolution of the air phase volume, pore connectivity, and estimating the

388   relative gas diffusion coefficient during successive wetting-drying cycles on the same soil

389   sample. Contrary to the use of other characterization techniques (e.g., measurements of the

390   gas diffusion coefficient with the one-chamber method), the hydric status of the soil has not

391   been modified by supplementary wetting-drying cycles, and N_2O entrapment has not been

392   disrupted.

393   We were able to measure an increase of the volume of the air phase connected to the soil

394   surface, and an increase of the pore connectivity and gas diffusion coefficient as the soil dried.

395   We used the Euler number as an indicator of the connectivity of the gas phase. Because this

396   metrics is highly affected by isolated pores, we based our interpretations on the Euler number

397   calculated for the pore space connected to the soil surface, rather than for the whole pore

398   space identified with imaging. Nitrous oxide emissions were lower in terms of intensity and

399   speed during the second drying cycle. Differences in the intensity of N_2O emissions were

400   attributed to differences in the water saturation, air-phase connectivity, and relative gas

401   diffusion coefficient, which led to more or less N_2O production, consumption, and entrapment

402   in soil. The speed of the N_2O release at the beginning of the drying phase depended on the

403   rate of increase of the air-filled pore volume, connectivity, and was especially well described

404   by the relative gas diffusion coefficient. Parameters of the soil structure were not able to

405   explain completely the intensity of N_2O emissions during drying, as N_2O production and

406   consumption factors modified the N_2O concentration gradient between the soil and the

407   atmosphere.

408   The soil structure can be seen as a factor of the N_2O flux intensity because the pore size

409   controls N_2O production by providing a favorable microbial habitat (i.e., aerobic status,

410   substrate availability, water potential), and because the pore tortuosity and connectivity to the

411   soil surface controls N_2O emission. This study highlighted the need to find and measure

412   dynamic indicators of the soil structure, to enhance our understanding of the dynamic nature

413   of N_2O emissions by soils. The results presented here are an illustration based on one soil

414   sample, but the methodology is widely applicable. Even if imaging with a coarse scanner

415 resolution provided valuable data, imaging techniques at a finer spatial resolution, able to

416 identify pores with diameter of approximately 50 μm, would allow refining these results.

417 **Acknowledgements**

References

425 **References**

426 Balaine, N., T.J. Clough, M.H. Beare, S.M. Thomas, E.D. Meenken, and J.G. Ross. 2013.

427   Changes in relative gas diffusivity explain soil nitrous oxide flux dynamics. Soil Sci.

428   Soc. Am. J. 77:1496–1505.

429 Ball, B.C. 2013. Soil structure and greenhouse gas emissions: A synthesis of 20 years of

430   experimentation. Eur. J. Soil Sci. 64:357–373.

431 Ball, B.C., I. Crichton, and G.W. Horgan. 2008. Dynamics of upward and downward N_2O and

432   CO_2 fluxes in ploughed or no-tilled soils in relation to water-filled pore space,

433   compaction and crop presence. Soil Tillage Res. 101:20–30.

434 Butterbach-Bahl, K., E.M. Baggs, M. Dannenmann, R. Kiese, and S. Zechmeister-

435   Boltenstern. 2013. Nitrous oxide emissions from soils: How well do we understand the

436   processes and their controls? Philos. Trans. R. Soc. B 368.

437 Castellano, M.J., J.P. Schmidt, J.P. Kaye, C. Walker, C.B. Graham, H. Lin, et al. 2010.

438   Hydrological and biogeochemical controls on the timing and magnitude of nitrous

439   oxide flux across an agricultural landscape. Glob. Change Biol. 16:2711–2720.

440 Ciais, P., C. Sabine, G. Bala, L. Bopp, V. Brovkin, J. Canadell, et al. 2013. Carbon and other

441   biogeochemical cycles. In: Stocker, T.F., D. Qin, G.K. Plattner, M. Tignor, S.K. Allen,

442   J. Boschung, et al., editors, Climate change 2013: The physical science basis.

443   Contribution of working group I to the fifth assessment report of the

444   intergovernmental panel on climate change. Cambridge University Press, Cambridge,

445   United Kingdom and New York, NY, USA. p. 465–570.

446 Clough, T.J., S.C. Jarvis, E.R. Dixon, R.J. Stevens, R.J. Laughlin, and D.J. Hatch. 1998.

447   Carbon induced subsoil denitrification of ^{15}N-labelled nitrate in 1 m deep soil

448   columns. Soil Biol. Biochem. 31:31–41.

449　Clough, T.J., R.R. Sherlock, and D.E. Rolston. 2005. A review of the movement and fate of

450　　　N_2O in the subsoil. Nutr. Cycl. Agroecosyst. 72:3–11.

451　Denef, K., J. Six, H. Bossuyt, S.D. Frey, E.T. Elliott, R. Merckx, et al. 2001. Influence of dry-

452　　　wet cycles on the interrelationship between aggregate, particulate organic matter, and

453　　　microbial community dynamics. Soil Biol. Biochem. 33:1599–1611.

454　Deurer, M., D. Grinev, I. Young, B.E. Clothier, and K. Müller. 2009. The impact of soil

455　　　carbon management on soil macropore structure: A comparison of two apple orchard

456　　　systems in New Zealand. Eur. J. Soil Sci. 60:945–955.

457　Doube, M., M.M. Klosowski, I. Arganda-Carreras, F.P. Cordelières, R.P. Dougherty, J.S.

458　　　Jackson, et al. 2010. BoneJ: Free and extensible bone image analysis in ImageJ. Bone

459　　　47:1076–1079.

460　Fierer, N., and J.P. Schimel. 2002. Effects of drying-rewetting frequency on soil carbon and

461　　　nitrogen transformations. Soil Biol. Biochem. 34:777–787.

462　Groffman, P.M., and J.M. Tiedje. 1988. Denitrification hysteresis during wetting and drying

463　　　cycles in soil. Soil Sci. Soc. Am. J. 52:1626–1629.

464　Gu, J.X., B. Nicoullaud, P. Rochette, D.J. Pennock, C. Hénault, P. Cellier, et al. 2011. Effect

465　　　of topography on nitrous oxide emissions from winter wheat fields in Central France.

466　　　Environ. Pollut. 159:3149–3155.

467　Guo, X.B., C.F. Drury, X.M. Yang, W.D. Reynolds, and R.Q. Fan. 2014. The extent of soil

468　　　drying and rewetting affects nitrous oxide emissions, denitrification, and nitrogen

469　　　mineralization. Soil Sci. Soc. Am. J. 78:194–204.

470　Heincke, M., and M. Kaupenjohann. 1999. Effects of soil solution on the dynamics of N_2O

471　　　emissions: A review. Nutr. Cycl. Agroecosyst. 55:133–157.

472   Hénault, C., and J.C. Germon. 2000. NEMIS, a predictive model of denitrification on the field

473   scale. Eur. J. Soil Sci. 51:257–270.

474   Jarvis, N.J. 2007. A review of non-equilibrium water flow and solute transport in soil

475   macropores: Principles, controlling factors and consequences for water quality. Eur. J.

476   Soil Sci. 58:523–546.

477   Kasteel, R., H.J. Vogel, and K. Roth. 2000. From local hydraulic properties to effective

478   transport in soil. Eur. J. Soil Sci. 51:81–91.

479   Katuwal, S., T. Norgaard, P. Moldrup, M. Lamandé, D. Wildenschild, and L.W. de Jonge.

480   2015. Linking air and water transport in intact soils to macropore characteristics

481   inferred from X-ray computed tomography. Geoderma 237–238:9–20.

482   Khalil, M.A.K., R.A. Rasmussen, and M.J. Shearer. 2002. Atmospheric nitrous oxide:

483   Patterns of global change during recent decades and centuries. Chemosphere 47:807–

484   821.

485   Letey, J., N. Valoras, A. Hadas, and D.D. Focht. 1980. Effect of air-filled porosity, nitrate

486   concentration, and time on the ratio of N_2O/N_2 evolution during denitrification. J.

487   Environ. Qual. 9:227–231.

488   Mangalassery, S., S. Sjögersten, D.L. Sparkes, C.J. Sturrock, J. Craigon, and S.J. Mooney.

489   2014. To what extent can zero tillage lead to a reduction in greenhouse gas emissions

490   from temperate soils? Sci. Rep. 4, 4586.

491   Mangalassery, S., S. Sjögersten, D.L. Sparkes, C.J. Sturrock, and S.J. Mooney. 2013. The

492   effect of soil aggregate size on pore structure and its consequence on emission of

493   greenhouse gases. Soil Tillage Res. 132:39–46.

494   McCarty, G.W., D.R. Shelton, and A.M. Sadeghi. 1999. Influence of air porosity on

495   distribution of gases in soil under assay for denitrification. Biol. Fert. Soils 30:173–

496   178.

497   Mikha, M.M., C.W. Rice, and G.A. Milliken. 2005. Carbon and nitrogen mineralization as

498   affected by drying and wetting cycles. Soil Biol. Biochem. 37:339–347.

499   Muhr, J., S.D. Goldberg, W. Borken, and G. Gebauer. 2008. Repeated drying-rewetting cycles

500   and their effects on the emission of CO_2, N_2O, NO, and CH_4 in a forest soil. J. Plant

501   Nutr. Soil Sci. 171:719–728.

502   Naveed, M., S. Hamamoto, K. Kawamoto, T. Sakaki., M. Takahashi, T. Komatsu, et al. 2013.

503   Correlating gas transport parameters and X-ray computed tomography measurements

504   in porous media. Soil Sci. 178:60–68.

505   Parker,   J.A.   2012.   Stack   Alignment   (Align3_TP).

506   http://www.med.harvard.edu/jpnm/ij/plugins/Align3TP.html.

507   Rabot, E., C. Hénault, and I. Cousin. 2014. Temporal variability of nitrous oxide emissions by

508   soils as affected by hydric history. Soil Sci. Soc. Am. J. 78:434–444.

509   Rasband, W.S. 1997-2014. ImageJ. U.S. National Institutes of Health, Bethesda, Maryland,

510   USA, http://imagej.nih.gov/ij.

511   Ravishankara, A.R., J.S. Daniel, and R.W. Portmann. 2009. Nitrous oxide (N_2O): The

512   dominant ozone-depleting substance emitted in the 21st century. Science 326:123–125.

513   Renard, P., and D. Allard. 2013. Connectivity metrics for subsurface flow and transport. Adv.

514   Water Resour. 51:168–196.

515   Ruser, R., H. Flessa, R. Russow, G. Schmidt, F. Buegger, and J.C. Munch. 2006. Emission of

516   N_2O, N_2 and CO_2 from soil fertilized with nitrate: Effect of compaction, soil moisture

517   and rewetting. Soil Biol. Biochem. 38:263–274.

518   Robertson, G.P. 1989. Nitrification and denitrification in humid tropical ecosystems: Potential

519   controls on nitrogen retention. In: J. Proctor, editor, Mineral nutrients in tropical forest

520   and savanna ecosystems. Blackwell Science, Oxford, U.K. p. 55–69.

521   Sammartino, S., E. Michel, and Y. Capowiez. 2012. A novel method to visualize and

522   characterize preferential flow in undisturbed soil cores by using multislice helical CT.

523   Vadose Zone J. 11:86–98.

524   Sanchez-Martin, L., A. Sanz-Cobena, A. Meijide, M. Quemada, and A. Vallejo. 2010. The

525   importance of the fallow period for N_2O and CH_4 fluxes and nitrate leaching in a

526   Mediterranean irrigated agroecosystem. Eur. J. Soil Sci. 61:710–720.

527   Schjønning, P., M. Lamandé, F.E. Berisso, A. Simojoki, L. Alakukku, and R.R. Andreasen.

528   2013. Gas diffusion, non-darcy air permeability, and computed tomography images of

529   a clay subsoil affected by compaction. Soil Sci. Soc. Am. J. 77:1977–1990.

530   Schlüter, S., A. Sheppard, K. Brown, and D. Wildenschild. 2014. Image processing of

531   multiphase images obtained via X-ray microtomography: A review. Water Resour.

532   Res. 50:3615–3639.

533   Schlüter, S., U. Weller, and H.J. Vogel. 2011. Soil-structure development including seasonal

534   dynamics in a long-term fertilization experiment. J. Plant Nutr. Soil Sci. 174:395–403.

535   Schmid, B., J. Schindelin, A. Cardona, M. Longair, and M. Heisenberg. 2010. A high-level

536   3D visualization API for Java and ImageJ. BMC Bioinformatics 11.

537   Sexstone, A.J., T.B. Parkin, and J.M. Tiedje. 1985. Temporal response of soil denitrification

538   rates to rainfall and irrigation. Soil Sci. Soc. Am. J. 49:99–103.

539   Smith, K.A. 1980. A model of the extent of anaerobic zones in aggregated soils, and its

540   potential application to estimates of denitrification. J. Soil Sci. 31:263–277.

541   van der Weerden, T.J., F.M. Kelliher, and C.A.M. de Klein. 2012. Influence of pore size

542   distribution and soil water content on nitrous oxide emissions. Soil Res. 50:125–135.

543   Vogel, H.J. 2008. QuantIm: C/C++ library for scientific image processing. Helmholtz Center

544   for Environmental Research, Halle, Germany.

545   Vogel, H.J, I. Cousin, and K. Roth. 2002. Quantification of pore structure and gas diffusion as

546   function of scale. Eur. J. Soil Sci. 53:465–473.

547   Vogel, H.J., U. Weller, and S. Schlüter. 2010. Quantification of soil structure based on

548   Minkowski functions. Comput. Geosci. 36:1236–1245.

549   Weier, K.L., J.W. Doran, J.F. Power, and D.T. Walters. 1993. Denitrification and the

550   dinitrogen/nitrous oxide ratio as affected by soil water, available carbon, and nitrate.

551   Soil Sci. Soc. Am. J. 57:66–72.

552   Weihermüller, L., J.A. Huisman, A. Graf, M. Herbst, and J.M. Sequaris. 2009. Multistep

553   outflow experiments to determine soil physical and carbon dioxide production

554   parameters. Vadose Zone J. 8:772–782.

555   Wildenschild, D., J.W. Hopmans, M.L. Rivers, and A.J.R. Kent. 2005. Quantitative analysis

556   of flow processes in a sand using synchrotron-based X-ray microtomography. Vadose

557   Zone J. 4:112–126.

558   Wollersheim, R., G. Trolldenier, and H. Beringer. 1987. Effect of bulk density and soil water

559   tension on denitrification in the rhizosphere of spring wheat (Triticum vulgare). Biol.

560   Fert. Soils 5:181–187.

561   World Meteorological Organization. 2007. Scientific assessment of ozone depletion: 2006,

562   global ozone research and monitoring project. Global Ozone Res. Monit. Project Rep.

563   50. World Meteorol. Organ., Geneva

564 **Figure captions**

565 **Fig. 1.** Schematic overview of the multistep outflow system for hydric control and nitrous

566 oxide measurements. Intensity values corresponding to air and water are zoomed in (c) and
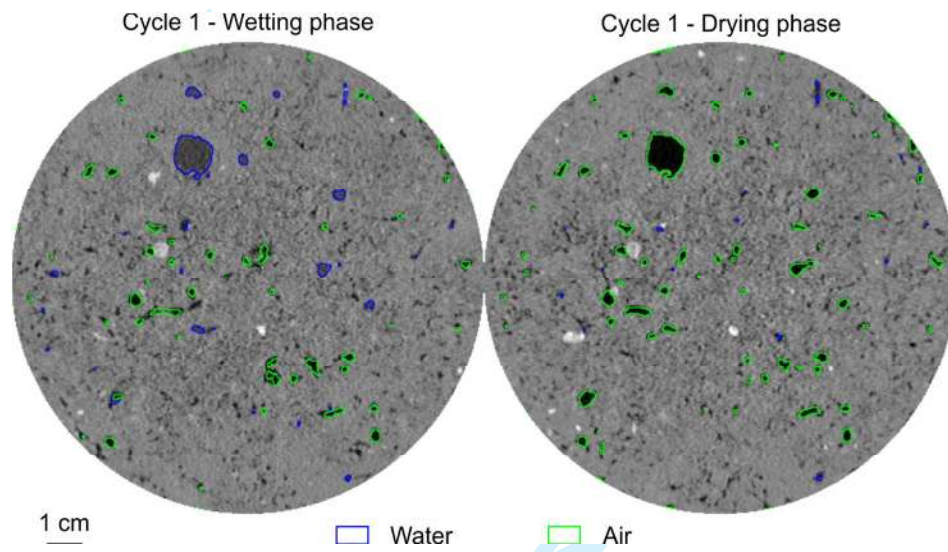
567 (d).

568 **Fig. 2.** Example of a gray scale slice with the segmented water and air, at the end of the

569 wetting phase and at the end of the drying phase.

570 **Fig. 3.** Evolution with time of the nitrous oxide fluxes and the matric potential measured by

571 the two tensiometers. Gray areas represent the drying phases, and white areas the wetting

572 phases. C1 is the first wetting-drying cycle, and C2 is the second wetting-drying cycle.

573 **Fig. 4.** Histograms of intensity values (16-bit), for (a) the first wetting-drying cycle, and (b)

574 the second wetting-drying cycle. Intensity values corresponding to air and water are zoomed

575 in (c) and (d).

576 **Fig. 5.** Three-dimensional distribution of the air phase (grey) and the water phase (blue) at the

577 end of the wetting phase and at the end of the drying phase for the two wetting-drying cycles.

578 **Fig. 6.** Evolution with time of (a) the air-filled and water-filled pore volume, and (b) the Euler

579 number of the total pore volume, (c) the air-filled pore volume, and (d) the Euler number of

580 the pores connected to the soil surface, for the first and second wetting-drying cycles. The

581 zero reference time is the beginning of the drying phase.

582 **Fig. 7.** Evolution with time of the relative gas diffusion coefficient of a 3-cm-thick subsample,

583 for the first and second wetting-drying cycles. The zero reference time is the beginning of the

584 drying phase.

585   **Tables**

586   **Table 1. Pearson correlation matrix of the indicators extracted from the segmented X-ray images.**

Variables	Euler number (T)	Euler number (S)	Air volume (T)	Air volume (S)	Water volume (T)	Gas diffusion coefficient (T)
Euler number (T)	1.00					
Euler number (S)	0.44	1.00				
Air volume (T)	−0.67	−0.91	1.00			
Air volume (S)	−0.72	−0.86	0.99	1.00		
Water volume (T)	0.65	0.77	−0.94	−0.95	1.00	
Gas diffusion coefficient (T)	0.01	−0.12	0.23	0.24	−0.41	1.00

T, calculated on the total air-filled pores identified; S, calculated on the air-filled pores connected to the soil surface.

587
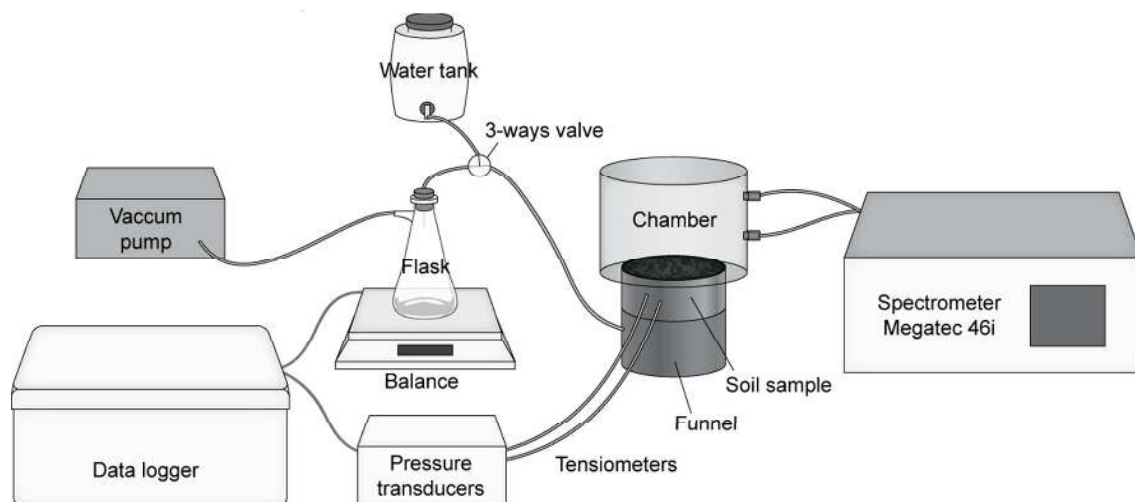
Fig. 1. Schematic overview of the multistep outflow system for hydric control and nitrous oxide measurements.

Fig. 2. Example of a gray scale slice with the segmented water and air, at the end of the wetting phase and at the end of the drying phase.
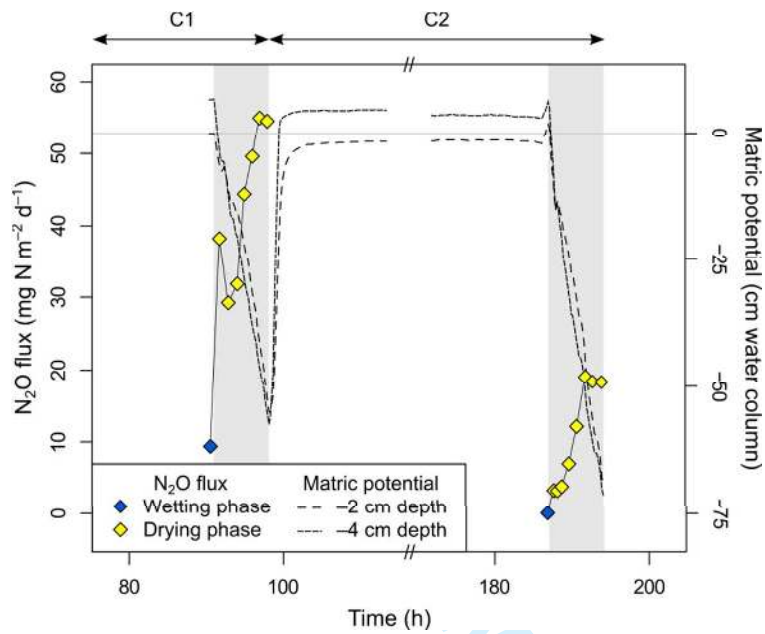
Fig. 3. Evolution with time of the nitrous oxide fluxes and the matric potential measured by the two tensiometers. Gray areas represent the drying phases, and white areas the wetting phases. C1 is the first wetting-drying cycle, and C2 is the second wetting-drying cycle.
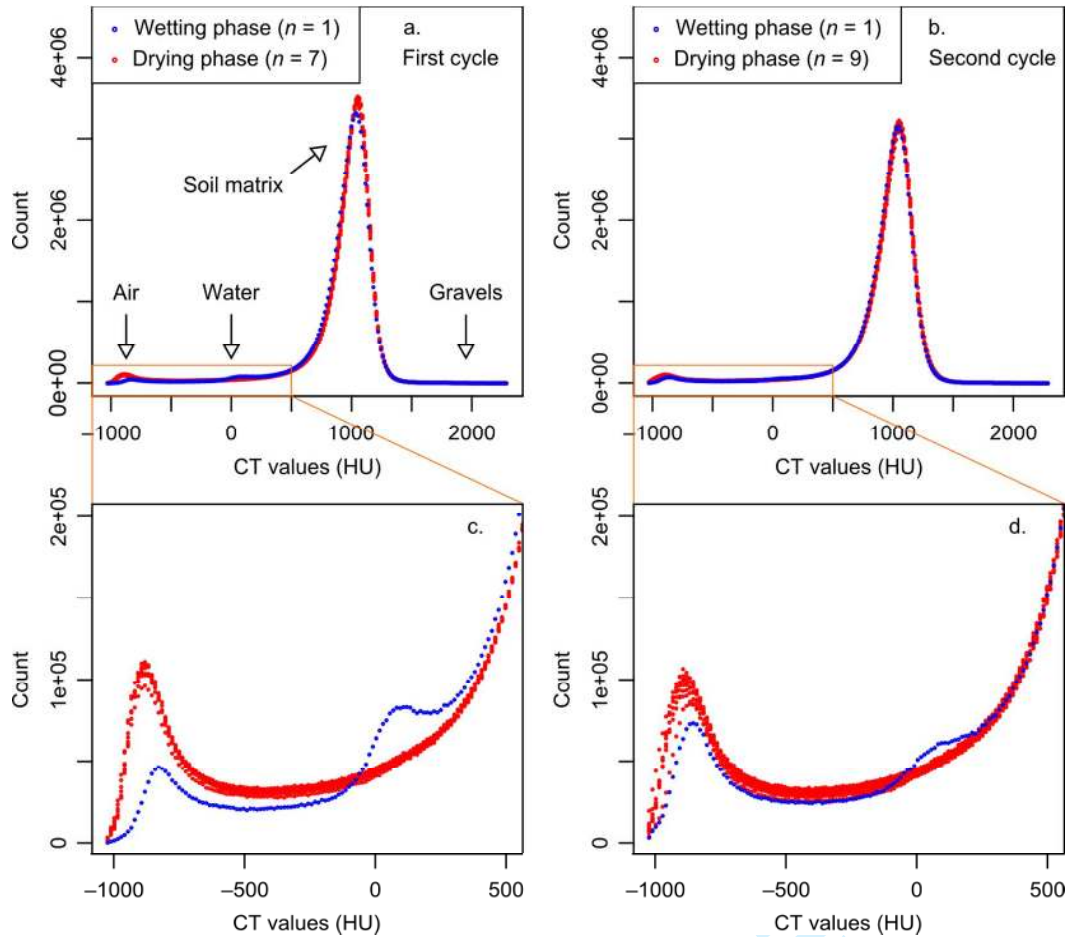
Fig. 4. Histograms of intensity values (16-bit), for (a) the first wetting-drying cycle, and (b) the second wetting-drying cycle. Intensity values corresponding to air and water are zoomed in (c) and (d).
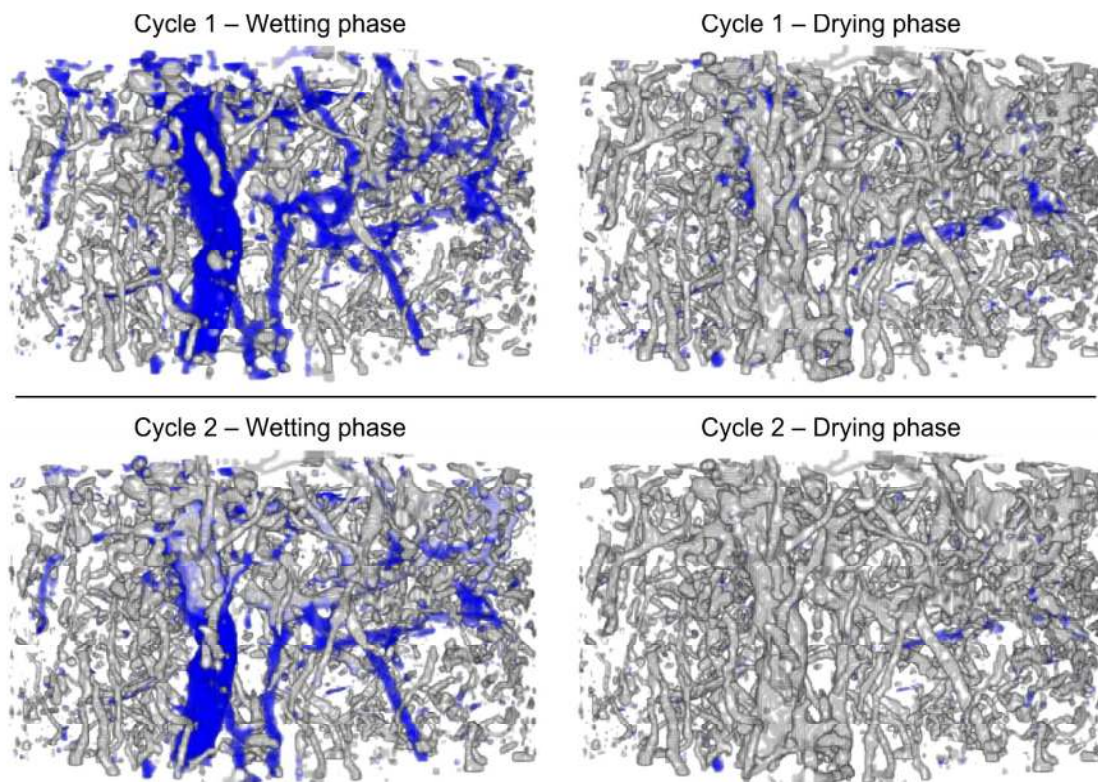
Fig. 5. Three-dimensional distribution of the air phase (grey) and the water phase (blue) at the end of the wetting phase and at the end of the drying phase for the two wetting-drying cycles.
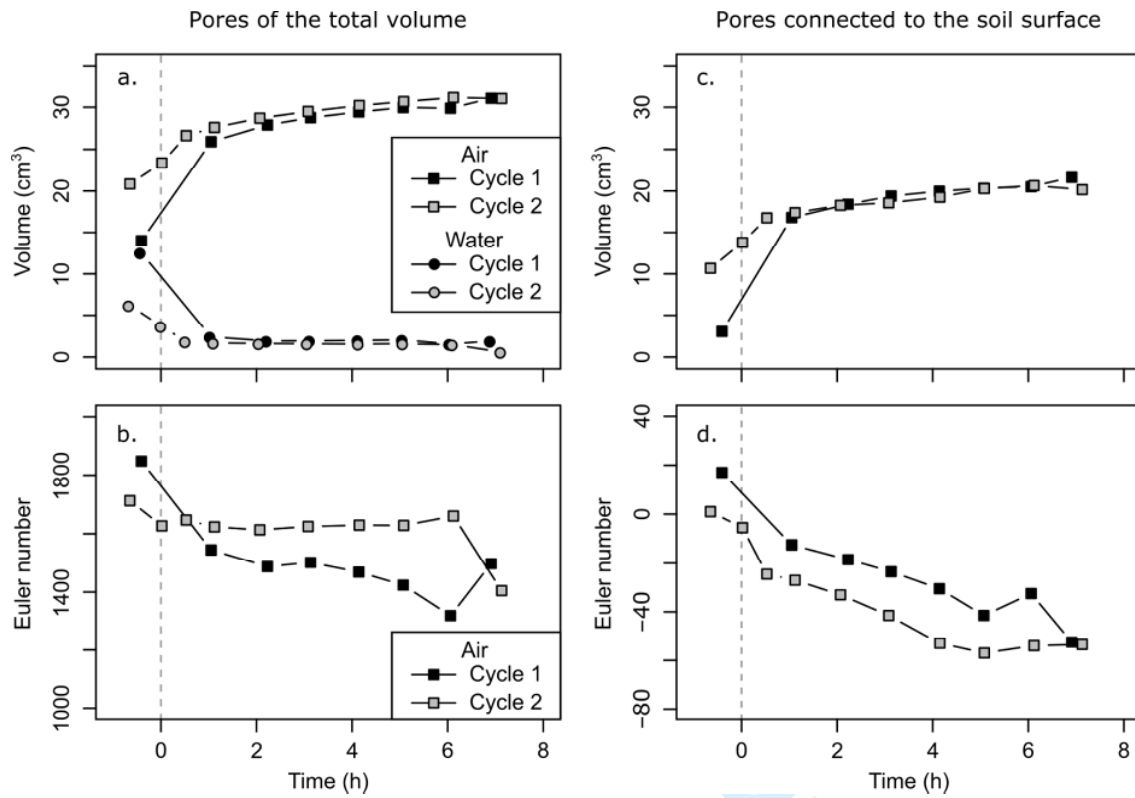
Fig. 6. Evolution with time of (a) the air-filled and water-filled pore volume, and (b) the Euler number of the total pore volume, (c) the air-filled pore volume, and (d) the Euler number of the pores connected to the soil surface, for the first and second wetting-drying cycles. The zero reference time is the beginning of the drying phase.
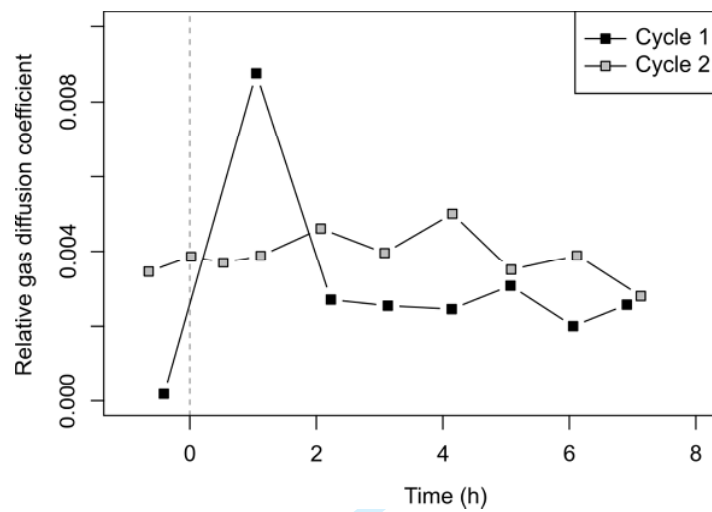
Fig. 7. Evolution with time of the relative gas diffusion coefficient of a 3-cm-thick subsample, for the first and second wetting-drying cycles. The zero reference time is the beginning of the drying phase.